J. Fluid Mech. (2007), *vol.* 571, *pp.* 235–263.
doi:10.1017/S002211200600334X Printed in the United Kingdom

Direct simulations of a rough-wall channel flow

By TOMOAKI IKEDA[1]† AND PAUL A. DURBIN[2]

[1]Department of Aeronautics and Astronautics, Stanford University, CA94305, USA
[2]Department of Aerospace Engineering, Iowa State University, IA 50011, USA

(Received 7 August 2005 and in revised form 25 June 2006)

In this study, we performed simulations of turbulent flow over rectangular ribs transversely mounted on one side of a plane in a channel, with the other side being smooth. The separation between ribs is large enough to avoid forming stable vortices in the spacing, which exhibits k-type, or sand-grain roughness. The Reynolds number Re_τ of our representative direct numerical simulation case is 460 based on the smooth-wall friction velocity and the channel half-width. The roughness height h is estimated as 110 wall units based on the rough-wall friction velocity. The velocity profile and kinetic energy budget verify the presence of an equilibrium, logarithmic layer at $y \gtrsim 2h$. In the roughness sublayer, however, a significant turbulent energy flux was observed. A high-energy region is formed by the irregular motions just above the roughness. Visualizations of vortical streaks, disrupted in all three directions in the roughness sublayer, indicate that the three-dimensional flow structure of sand-grain roughness is replicated by the two-dimensional roughness, and that this vortical structure is responsible for the high energy production. The difference in turbulence structure between smooth- and rough-wall layers can also be seen in other flow properties, such as anisotropy and turbulence length scales.

1. Introduction

Rough-wall turbulence arises in many applications, such as turbo-machinery, electronics cooling, and vegetation canopies. Most walls are effectively rough in the high-Reynolds-number limit. In a smooth-wall boundary layer, the viscous sublayer exhibits a high impedance for momentum and heat transfer between flow and a surface, which characterizes the near-wall behaviour of smooth-wall turbulence. In this near-wall region, the Kolmogoroff length scale becomes the same order as, or larger than, the distance from the wall, so that viscous diffusion, rather than eddy diffusion, is dominant. Surface roughness disturbs this viscous layer structure, producing irregular turbulent motions and affecting the transfer rates.

For random roughness, the origin may be defined as the mean height of the roughness elements. Then, the turbulent kinetic energy (TKE) at $y = 0$ is not zero, unlike at a non-slip smooth surface. In a macroscopic sense, this implies a need to consider kinetic energy transfer to and from the rough surface, which would contradict the equilibrium boundary condition commonly adopted in roughness modifications of turbulence models (for example, see Arora, Kuo & Razdan 1982; Lee 1996). The role of a rough surface should be identified as either sink or source for TKE, depending on the sign of an energy flux in the wall-normal direction at the surface.

† Present address: Japan Aerospace Exploration Agency, Chofu, Tokyo 182-8522, Japan.

Our objective has been to understand turbulence modifications for their relevance to statistical closure models on the rough-wall boundary layer via direct numerical simulations (DNS), especially in terms of the TKE flux in a near-wall region.

Since the roughness height h is a parameter in determining the effective roughness state when normalized in wall units by friction velocity u_τ and molecular viscosity ν, h^+ may become large enough at a high Reynolds number, even if h is infinitesimal compared to a characteristic length of the field, L. This can be understood from the following relation:

$$h^+ = \frac{hu_\tau}{\nu} = \frac{h}{L} Re_\tau \to \infty \qquad \text{as} \quad Re_\tau \to \infty. \tag{1.1}$$

As h^+ increases, the flow state is altered. Based on sand-grain roughness experiments for pipe flows by Nikuradse (1933), a rough-wall turbulent flow can be classified as *fully rough*, for $h^+ > 70$. In general, the critical roughness-height varies with geometrical configurations; for instance, this critical height may decrease down to $h^+ \simeq 10$ for two-dimensional rib-type roughness, as shown by Bandyopadhyay (1985). The fully rough state means that the flow reaches a certain limit at the critical Reynolds number, if the roughness geometry is fixed; beyond that, the flow becomes independent of molecular viscosity, which is indicated by the modified logarithmic law (Tennekes & Lumley 1972; Perry & Joubert 1963; Perry, Schofield & Joubert 1969; Schlichting 1979):

$$\frac{U}{u_\tau} = \frac{1}{\kappa} \log\left(\frac{y}{h}\right) + B, \tag{1.2}$$

where κ is the von Kármán constant, y is the distance from the wall, and B is a reformed additive constant. Since historically the sand-grain roughness had been extensively studied, the *equivalent sand-grain height* is defined through (1.2). For sand-grain roughness, $B = 8.5$ has been obtained for the fully rough state. In general, once B is determined for given h and Reynolds number, the equivalent sand-grain height h_{sand} for the rough surface is obtained via:

$$B = 8.5 + \frac{1}{\kappa} \log\left(\frac{h}{h_{sand}}\right). \tag{1.3}$$

In addition to the modification of an additive constant, we could shift the origin of the logarithmic function for a better fit of velocity distributions above rough walls to a log-profile. This has been done along with atmospheric studies as well as laboratory measurements (Hanjalić & Launder 1972; Jackson 1981; Bandyopadhyay 1985; Raupach, Antonia & Rajagopalan 1991).

Two types of roughness

In an engineering context, two types of roughness have been recognized, depending on the surface configuration. One is called 'k' type roughness, which is represented by sand-grain roughness. This is characterized by unstable eddies that have a length scale proportional to k, or roughness height, formed behind a roughness element. The eddies shed into the flow produce three-dimensional turbulent motions, and form the roughness sublayer structure. Three-dimensional irregular protrusions are also supposed to be included in this type. In laboratory work, Ligrani & Moffat (1986), Perry, Henbest & Chong (1986), Krogstad, Antonia & Browne (1992), Krogstad & Antonia (1994), Shafi & Antonia (1997) investigated rough-wall boundary layers of regularly configured k-type surfaces. The other type of roughness is referred to as 'd' type, characterized by the two-dimensional geometry of rectangular elements; the

spacing between them is about the same order as the element height. Its flow pattern is represented by stable vortices confined in narrow cavities. Therefore, the interaction between roughness and the outer flow region is relatively restricted (Perry *et al.* 1969; Bandyopadhyay 1985).

For the roughness comprising cylindrical rectangular ribs, the spacing between them, w, is a determinative parameter, indicating whether it is k-type or d-type. For narrow cavity spacing, d-type roughness is achieved as has been explained, whereas k-type behaviour is observed for wider rib separation. In the experimental study by Bandyopadhyay (1985), it is reported that $w \simeq 3h$ is large enough to lead to k-type roughness, whereas $w \lesssim h$ shows d-type roughness. Leonardi *et al.* (2003*b*) and Nagano, Hattori & Houra (2004) also numerically investigated the effect of this cavity spacing for rectangular rib roughness. The experiment conducted by Raupach (1981) is the example of various two-dimensional cylindrical geometries of k-type roughness.

Efforts to resolve the roughness sublayer

In experimental studies, the major problem in obtaining turbulence statistics within a roughness sublayer is measurement error due to the high turbulence intensities near roughness elements; this measurement difficulty is inherent in rough-wall turbulence. Hence, the roughness sublayer has been studied in only a few cases of engineering laboratory work, excepting cavity flows of d-type roughness (Perry, Schofield & Joubert 1969; Djenidi, Elavarasan & Antonnia 1999). In meteorological work, on the other hand, turbulence structure within a canopy has been resolved to some degree. When statistical quantities within roughness are expressed, horizontal averaging is often used to remove the fluctuations in a vegetation wake. One-dimensional functions on height are derived in those cases (Wilson & Shaw 1977; Raupach & Shaw 1982).

Since rough-wall turbulence is complex in terms of its geometrical configuration and flow structure, a numerical simulation to resolve the flow down to the roughness sublayer may have been expensive even for simplified roughness geometries. Several DNS cases have been reported for wall roughness. De Angelis, Lombardi & Banerjee (1997) and Cherukat *et al.* (1998) studied two-dimensional wavy walls at relatively low Reynolds numbers. Rectangular rib-roughness has also been investigated in DNS studies (Miyake, Tsujimoto & Nakaji 2001; Ashrafian & Andersson 2003; Leonardi *et al.* 2003*b*; Nagano *et al.* 2004). In their work, the rib spacing was held large enough to attain k-type roughness at various roughness heights, ranging from $h^+ = 13.6$ (Ashrafian & Andersson 2003) to $h^+ = 90$ (Leonardi *et al.* 2003*b*). As shown by Bandyopadhyay (1985), $h^+ \simeq 10$ is a critical value for a fully rough state; hence, all these calculations may be assumed to be fully developed rough-wall simulations. In addition, Leonardi *et al.* (2003*b*) examined the wide variety of w/h to investigate the rib spacing effect parametrically.

There are several LES studies for flow over bluff-body obstacles using a finite-difference approach (e.g. Yang & Ferziger 1993; Shah & Ferziger 1998; Cui, Patel & Lin 2003), although not all of them were conducted primarily for wall roughness. Shah & Ferziger (1998) simulated flow over a cube mounted on a wall. Their study shows coherent vortical structures, which include periodic horseshoe-vortex shedding around a cube in the time-dependent field. In our study, however, the features seen in § 5 are different from their three-dimensional obstacle flow.

Research objectives

For a better understanding of rough-wall turbulence, detailed flow structures in the vicinity of a roughened surface should be clarified, as well as those in the

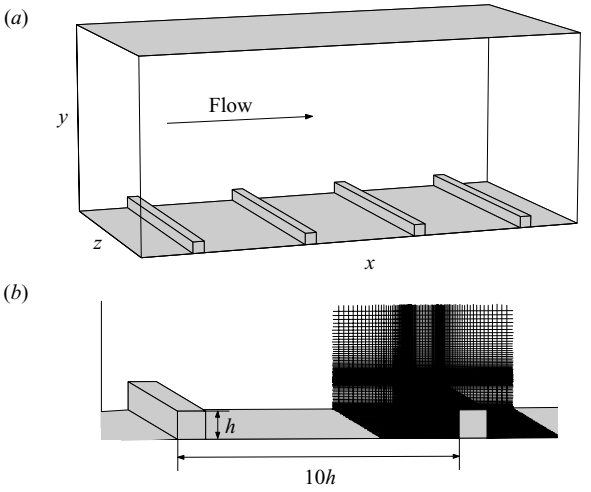

FIGURE 1. (*a*) Asymmetric channel geometry of the representative case. (*b*) Configuration of rib roughness and a subset of the numerical grid.

outer region above the roughness sublayer. We perform direct numerical simulations of a rough-wall turbulent flow for this purpose, since it is well suited in terms of the resolution of data sampling and visualizations of both instantaneous and averaged flow fields. The fully rough turbulent flow of k-type roughness is numerically reproduced, which is distinguished by irregular unsteady flow motions. The Reynolds number we select here should be high enough to reach a fully rough state, by carefully examining the numerical resolution in the roughness sublayer. In the simulation, the fundamental mechanism of k-type roughness will be clarified. The three-dimensional vortical structure near roughness elements will be captured through data analysis and visualizations. It must be examined in conjunction with a TKE flux on a rough surface, since the vortical motion is responsible for the major production of TKE. Also, through the post processing of statistical data, the roughness effects on Reynolds stress and TKE budget are estimated. The equilibrium assumption, which is common in statistical models, is re-assessed. The energy balance on a rough surface is carefully examined, to ascertain whether the wall roughness serves as an energy sink or source for the outer layer.

2. Computational geometry and numerical method

For the simulation of a rough-wall turbulent flow, two-dimensional rib roughness is employed. Cylindrical rectangular ribs are mounted on one side of a plane channel to represent strip roughness, aligned in the spanwise direction, while the other side is left smooth. As a representative case, a square cylinder is chosen for rib roughness; the spacing between two ribs is $9h$, where h is the square rib height, which defines one wavelength of geometrically periodic roughness as $10h$. The wavelength is large enough for the attached square ribs to reproduce k-type roughness, since the reattachment of boundary-layer separation occurs within the spacing (Bandyopadhyay 1985). A complete view of the representative channel geometry and a subset of the numerical grid is shown in figure 1. The asymmetric channel chosen here was experimentally investigated by Hanjalić & Launder (1972). In our DNS study, periodic boundary conditions are applied in the streamwise direction

as well as in the spanwise direction. The flow is driven by a prescribed mean pressure gradient. In the representative configuration, four ribs are mounted to form a rough wall. The domain size is given as $(L_x, L_y, L_z) = (40h, 17h, 20h)$ in the streamwise, wall-normal, and spanwise directions, respectively.

The way in which the randomness of roughness geometry affects turbulence quantities is also of interest. To imitate random roughness, we conducted another case of rectangular rib roughness with two rib-heights. Unevenness of rib height is imposed by alternatively increasing and decreasing the original square rib height h by 15 % to $0.85h$ and $1.15h$, so that the average of roughness heights remains equal to h. The other geometrical parameters, such as the rectangular-rib width, rib-spacing, and channel width, remain the same, h, $9h$ and $17h$, respectively. The same mean pressure gradient as in the cases with the square rib roughness is applied.

The governing equations are the incompressible Navier–Stokes equations,

$$\frac{\partial U_i}{\partial t} + \frac{\partial (U_i U_j)}{\partial x_j} = -\frac{\partial P}{\partial x_i} + \nu \frac{\partial^2 U_i}{\partial x_j \partial x_j}, \tag{2.1}$$

$$\frac{\partial U_j}{\partial x_j} = 0, \tag{2.2}$$

where U_1, U_2 and U_3 (or U, V and W) are velocities in the x_1 (streamwise), x_2 (normal) and x_3 (spanwise) directions (or x, y and z), respectively, P is pressure, and ν is molecular viscosity. To advance the solution in time, a fractional step method (Kim & Moin 1985) is employed with a semi-implicit approach; the time advancement of the momentum equations is the hybrid of an explicit third-order Runge–Kutta scheme and an implicit second-order Crank–Nicolson scheme (Spalart 1987). At each substep of the semi-implicit scheme, the momentum equations are advanced with pressure terms left unchanged. Then, the intermediate velocity is projected onto a divergence-free field to satisfy the continuity equation (2.2) through the pressure correction function, which obeys a Poisson equation. The governing equations are spatially discretized with a second-order centred difference scheme on a rectangular grid, where a three-dimensional staggered mesh is employed with a finite-difference formulation, unequally spaced in the x- and y-directions. Still the numerical scheme can use the homogeneity of the grid spacing in the z-direction to reduce the three-dimensional Poisson equation to a set of decoupled two-dimensional Helmholtz equations through a Fourier decomposition (Akselvoll & Moin 1995). Each Fourier mode is solved with a multigrid method to accelerate the convergence of the iterative procedure.

As seen in figure 1(*b*), the numerical grid is densely allocated near walls, in both the streamwise and wall-normal directions, to sufficiently resolve a rough-wall boundary structure of turbulence motions. Since the grid is fitted to the rib surface, we do not require a forcing-function technique that was employed in several other studies to represent a roughness element (e.g. Miyake *et al.* 2001; Leonardi *et al.* 2003*b*). Rather, non-slip boundary conditions are applied directly to momentum equations on the rib surface, as well as on the upper and lower channel walls. To avoid the restriction of the Courant–Friedrichs–Lewy condition due to the grid being finely placed in the streamwise and wall-normal directions near a square rib, both the convective and viscous terms in these directions are implicitly treated; the spatial differences in the spanwise direction are explicitly solved. As for the discretization of convective terms, it turns out that the mesh stretching in the streamwise direction may severely disturb turbulent eddies, and therefore, adversely affect resultant statistical quantities. In our

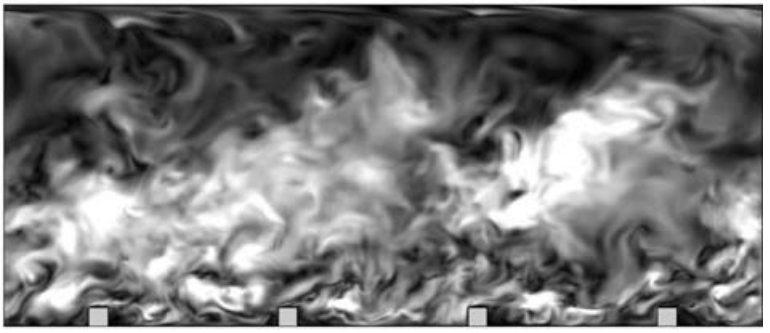

FIGURE 2. Instantaneous velocity fluctuation, $(u^2 + v^2 + w^2)^{1/2}$, in the (x, y)-plane of the entire domain. Grey scales range from 0.0 (black) to 4.0 (white) in wall units, normalized by the friction velocity at the rough-wall side, u_{τ_R}.

ribbed-wall DNS study, the convective scheme was carefully examined and tested to minimize this mesh stretch error. The formula employed is written in the conservative form for momentum, and reduces to the kinetic-energy conserving form in the inviscid limit if the numerical mesh is equally spaced. The details of the spatial discretization are presented in Ikeda & Durbin (2004).

3. Summary of numerical results

We carried out a full turbulent simulation on square rib roughness, referred to as Case F–1. The adequacy of grid resolution for this simulation is examined and confirmed through an extensive grid-independence study; the details and additional sampled-data sets can be found in Ikeda & Durbin (2002). An instantaneous view of velocity fluctuation in an (x, y)-plane is shown in figure 2. Near the rough-wall surface, eddies with length scales comparable to the roughness height can be recognized. In the middle of the channel, a large volume of high-velocity fluctuation is formed away from the wall, and convected downstream with the mean flow. The smooth-wall side is relatively inactive except for the streaks near the upper surface.

As a reference case, we name the experimental study by Hanjalić & Launder (1972) Case H–L. The experiment was conducted at various Reynolds numbers ranging from 18 500 to nearly 80 000 based on the maximum velocity and half the distance between the planes, while the corresponding Reynolds number of our fully resolved DNS case is about 8200. Although the Reynolds numbers of their study are more than twice, up to several times, as high as those of our numerical simulations, their data serve to validate the numerical results; some statistical results do not exhibit obvious Reynolds-number dependence. When compared to our DNS case, however, the results at the lower Reynolds numbers are used.

The ratio of shear forces acting on the rough and smooth walls is about 4:1, which agrees with that reported in Case H–L. On the rough-wall side, the dominant drag is the pressure force on the side faces of the ribs; in fact, the mean viscous stress on the surface provides a negative contribution owing to recirculation around the rib, while the pressure drag is nearly 105 % of the total force. Therefore, τ_R denotes the mean drag force per unit area on the rough wall, while τ_S is solely the mean viscous force per unit area on the smooth wall.

On the same geometry, we performed two-dimensional steady-state RANS calculations with an eddy-viscosity model, not only to validate our DNS results, but

Case	L_x/h	Grid size	$\tau_R : \tau_S$	Re_b	Re_{τ_S}	h_R^+
F–1	40	$1024 \times 352 \times 192$	4.05	6520	460	109
M–2	60	$864 \times 288 \times 128$	3.71	6730	478	108*
RANS	10	$112 \times 161 \times 1$	2.70	8110	539	104

* The average of two roughness heights; each height is 92 and 125 wall units, respectively.

TABLE 1. Summary of numerical simulation for rib roughness. Re_b is the Reynolds number based on the bulk velocity and half the channel width, $Re_b = U_{bulk} L_y / 2\nu$.

$\Delta x_{S\,min}^+$	$\Delta x_{S\,max}^+$	$\Delta y_{S\,min}^+$	$\Delta y_{S\,max}^+$	Δz_S^+
0.20	6.2	0.20	7.6	5.6

TABLE 2. Grid spacings for the fully resolved Case F–1. Wall units are based on the friction velocity of the smooth-wall side, u_{τ_S}.

also to examine the performance of turbulence models. The RANS solver employed here uses the artificial compressibility scheme (Rogers & Kwak 1990); the $\overline{v^2}$–f model (Durbin 1991) is implemented for eddy viscosity in the solver. The employed model constants and treatment of no-slip boundaries are summarized in Durbin (1995). Since $h_R^+ = h/\tau_R > 100$ has been achieved in each case, the roughness height is supposed to be large enough to produce the fully rough state.

In addition, a turbulent simulation on rectangular rib roughness with non-uniform height, Case M–2, is considered in order to examine an uneven-roughness effect as described in § 2. The streamwise domain length L_x, grid size and other flow properties are summarized in table 1. In all the DNS cases, the spanwise length is $20h$. Although the grid resolutions in the above two cases are different, we confirmed through a grid-independence study that the grid size used in Case M–2 did not exhibit significant effects on obtained statistical data, when the same level of coarser grid resolution was applied to the square rib roughness compared with the fully resolved result, Case F–1.

The numerical mesh used in the simulations is unequally spaced in the streamwise and wall-normal directions, and homogeneous in the spanwise direction. For Case F–1, table 2 summarizes the mesh spacings in each direction, normalized in wall units using the friction velocity on the smooth-wall side. If the rough-wall friction velocity is used for normalization, the values become about twice as large as those shown in table 2. In the wall-normal direction, the minimum spacing comes to both sides of the channel, and also on the top of the square rib. In the streamwise direction, the spacing is minimized on the front and back sides of the rib, and reaches a maximum at the middle between the ribs. The maximum grid stretching ratio is 1.1 in both inhomogeneous directions, just above the rib and near the smooth wall, and also near the upstream and downstream sides of the rib. The region within the rib roughness is finely resolved with a low grid stretching ratio.

4. Averaged results

4.1. *Mean velocity field*

Figure 3 shows the distribution of the mean streamwise velocity, averaged in the streamwise direction and normalized by $U_{max} = \langle \overline{U} \rangle|_{max}$ of the DNS case, where the overbar and the angle brackets denote ensemble average and streamwise average,

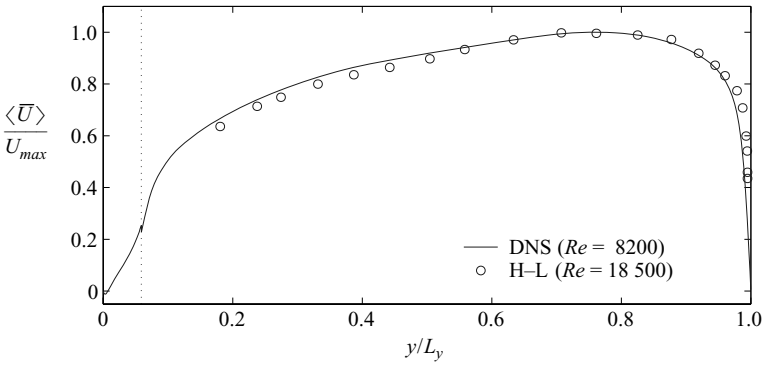

FIGURE 3. Mean velocity profiles normalized by U_{max} for Case F–1 and H–L. The dotted line indicates the square roughness height, $y = h$.

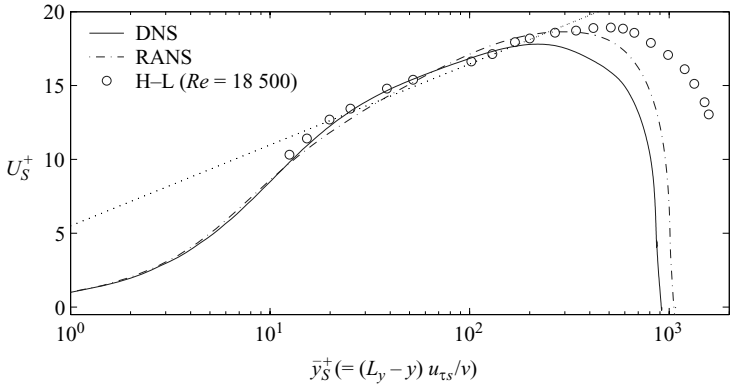

FIGURE 4. Smooth-wall mean velocity profiles on a logarithmic scale. $U_S^+ = \langle \overline{U} \rangle / u_{\tau_S}$. The dotted line is a smooth-wall log-law, $U_S^+ = (1/\kappa) \ln \tilde{y}_S^+ + A$, where $\kappa = 0.42$; the additive constant $A = 5.5$.

respectively. The Case H–L result at $Re = 18\,500$ is also shown. Although the Reynolds number of the DNS case is lower than for H–L, the mean velocity profiles agree well, after the normalization by U_{max}.

The zero-turbulent shear location does not coincide with the zero-mean velocity shear location, at which $\langle \overline{U} \rangle$ takes its maximum in the asymmetric channel, as pointed out by Hanjalić & Launder. U_{max} is given at $y/L_y = 0.76$, whereas $\langle \overline{u}\overline{v} \rangle$ reaches zero at $y/L_y = 0.81$ in our DNS case; both the positions are closer to the smooth-wall side than the experimental data, about 0.70 and 0.79, respectively.

Since the zero-turbulent shear location is close to the smooth-wall side, the interaction of turbulent motions from both sides of the channel occurs near that wall. Because of this, the smooth-wall side does not reach the asymptote of channel flow turbulence at a high Reynolds number, although the Reynolds number of our DNS case is sufficiently high. The maximum of TKE production is about 0.22 in wall units normalized by $u_{\tau_S}^4/\nu$, instead of 0.25. The distance between the smooth wall and the zero-shear location is about 180 in wall units normalized by ν/u_{τ_S}.

Velocity profiles on a logarithmic scale, whose origin is taken on the smooth wall, are shown in figure 4. Since Case H–L is at a higher Reynolds number than the

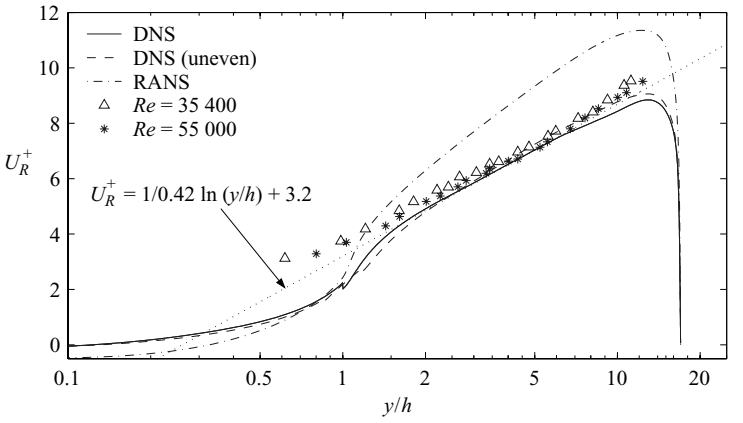

FIGURE 5. Rough-wall mean velocity profiles on a logarithmic scale. $U_R^+ = \langle\overline{U}\rangle/u_{\tau_R}$. The dotted line is an empirical equation proposed by Hanjalić & Launder (1972).

numerical simulations, the maximum velocity of H–L in wall units is larger than the DNS cases. Nevertheless, each case replicates the logarithmic law on a smooth wall.

Rough-wall velocity profiles on a logarithmic scale are shown in figure 5. The DNS results are compared to the H–L experimental data and the RANS solution with the $\overline{v^2}$–f model. The velocity is normalized by u_{τ_R}. Both the even and uneven DNS cases show a log-dependence with the slope of $1/\kappa$ above $y \approx 2h$. A modified logarithmic function, proposed by Hanjalić & Launder,

$$U_R^+ = \frac{1}{\kappa} \log\left(\frac{y}{h}\right) + 3.2, \tag{4.1}$$

agrees well with our DNS profile. This is the case where $B = 3.2$ in (1.2). In figure 5, we needed no origin shifting for a better log-law velocity profile fit. By applying least-squares fitting, we found the optimum displacement height of the origin greatly depends on the integration range. Although Hanjalić & Launder suggested $-0.4h$ for the displacement height, our data indicate that the additive constant, $B = 3.2$, employed in (4.1), is achieved without any displacement by the fitting. Also, compared to the roughness function obtained in the DNS study of a rib-roughened channel by Leonardi *et al.* (2003*b*), their velocity-profile fitting corresponds to $B \simeq 3.2$ for the case $w/h = 7$, where w is the spacing between ribs, if their roughness height h^+ is estimated to be 90 wall units as they provided.

If we apply (1.3) to obtain the equivalent sand-grain height, h_{sand}, for this rib roughness, it would reach nearly 1000 wall units, owing to a relatively low additive constant, $B = 3.2$. However, this is only a consequence from logarithmic velocity profile fitting way above the roughness sublayer. Equivalent sand-grain roughness is an estimate that correlates a given geometrical configuration and an obtained velocity profile, based on the experiments of sand-roughened pipe flow. Although it is widely used as a measure for wall roughness, it should be noted that h_{sand} does not directly indicate a physically significant level of rough-wall flow structure.

A RANS solution is included in figure 5. It is the streamwise average of a solution for flow over the detailed rib geometry. This should not be confused with RANS models that are modified for unresolved roughness. The RANS does show a log-dependence, but the slope does not match the reciprocal of the Kármán constant. In addition to the $\overline{v^2}$–f model, the Spalart–Almaras model (Spalart & Allmaras 1994)

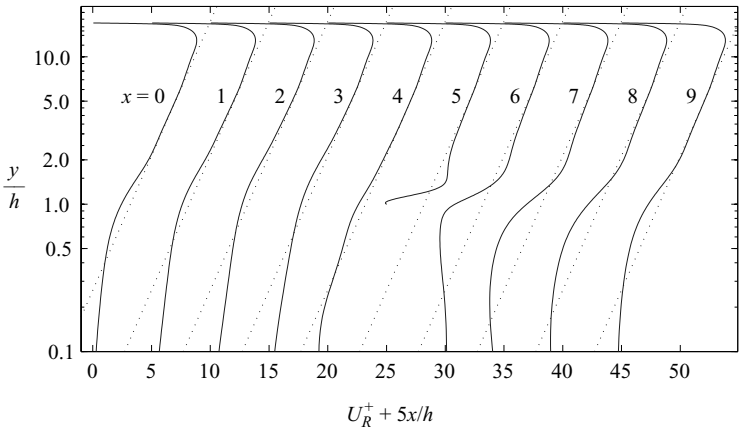

FIGURE 6. Rough-wall velocity profiles on a logarithmic scale at various x locations for the DNS case. The log function of (4.1) is also shown with dotted lines. Rib roughness exists in $4.5 \leqslant x/h \leqslant 5.5$, $0 \leqslant y/h \leqslant 1$.

was also solved, with an essentially identical result: the streamwise-averaged flow had a log-layer velocity profile that went above the data, with the wrong slope. In addition to these eddy viscosity models, Seo (2004) applied Reynolds-stress models to the same flow configuration, with almost the same result. Note that, in part, the discrepancy reflects an error in the pressure drag on the rough-wall side, since that enters the normalization.

The reason for the inaccurate RANS prediction could be that the eddies seen near the surface, as will be shown in figures 13 and 14, are rather different. Next to a smooth wall, they are elongated parallel to the surface; above the rib roughness, they are choppier and lift away from the wall. Models calibrated with smooth-wall data may not have the correct empiricism to capture the averaged flow over rib roughness when the geometry is fully resolved. Models that are modified for random roughness do not attempt to capture the flow in between roughness elements. They are applicable above the roughness and often have the correct log-layer displacement built into them (e.g. Durbin *et al.* 2001).

Figure 6 shows the distribution of $\overline{U}$ profiles on a logarithmic scale, for various x locations over one period of roughness geometry. Deviations from the mean profile can be recognized near the surface, below $y \simeq 2h$ to $4h$; however, even near the rib roughness, departure from the log-function is trivial at $y > 2h$. Above the region directly influenced by the roughness, the log-dependence of velocity profiles is observed at all locations in the channel.

4.2. *Streamlines and reattachment lengths*

The streamlines of the averaged two-dimensional velocity field of the DNS result, Case F–1, are shown in figure 7, as well as the steady state RANS result. In the DNS case of figure 7(a), several separation–reattachment (SR) regions are developed. Each zone is bounded by the non-slip walls and the zero-velocity lines that are denoted by a dashed line. The primary downstream SR region, whose separation occurs downstream of the rib top, has its reattachment at about the middle of rib spacing, or $4.5h$ behind the back face of a square rib. In the upstream region of the rib roughness, a smaller SR zone is formed, as well as a secondary SR region in the downstream. In addition to these, a thin SR region on the rib-top can be recognized in the figure. In

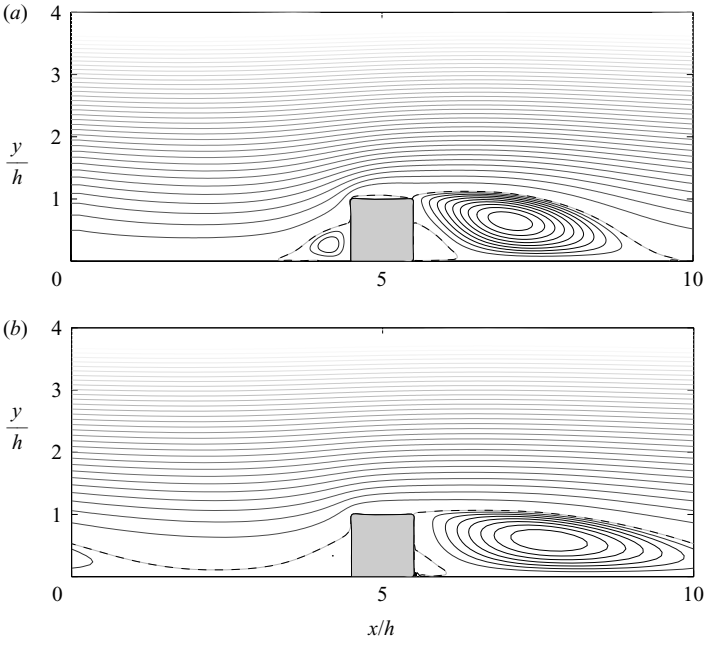

FIGURE 7. Streamlines of an averaged field around a square rib for: (*a*) DNS (F–1); (*b*) steady-state RANS (v^2–f). Dashed lines denote zero-velocity. One contour level indicates $3.33 \times 10^{-1}\%$ of the total mass flux in the positive flux region, and $4.50 \times 10^{-2}\%$ in the positive.

other DNS studies for similar flow geometries, Leonardi *et al.* (2003*b*) reported $4.8h$ for the reattachment length in their $w/h \geqslant 7$ cases, while the result by Ashrafian & Andersson (2003) did not show apparent reattachment for the primary recirculation bubble at $w/h = 7$. On the other hand, the streamlines obtained by Miyake *et al.* (2001) show that the reattachment of the primary SR region occurs directly on the upstream side of a rib, not on the bottom of the rib spacing, which is quite different from the above cases including our result, while $w/h \simeq 6$. This difference can be attributed to the Reynolds-number dependence of flow structure within roughness. Although the study by Bandyopadhyay (1985) indicates that $h^+ \simeq 10$ may be large enough to reach the fully rough state for this typical roughness configuration, still a difference of mean velocity profiles is observed in the numerical studies performed at different Reynolds numbers and roughness heights, on a similar geometry.

Compared to our DNS solution, the steady-state RANS shows a different result: the primary downstream SR region is elongated along the bottom wall, and combined into the upstream region. Whereas the DNS solution is the average of an unsteady flow field, only a steady-state solution can be obtained through the RANS simulation. Even if a second-order temporal accuracy is retained with a sufficiently small time-step size, no unsteady motion is observed. However, if RANS is used for flow past an obstacle, not attached to a plane, a periodic vortex shedding may be reproduced (e.g. Durbin 1995). If unsteady motions are reproduced in RANS, it can represent additional Reynolds stress, and the downstream SR length would be shortened. Nevertheless, unsteady solutions cannot be obtained in two-dimensional RANS simulation when an obstacle is mounted on a surface.

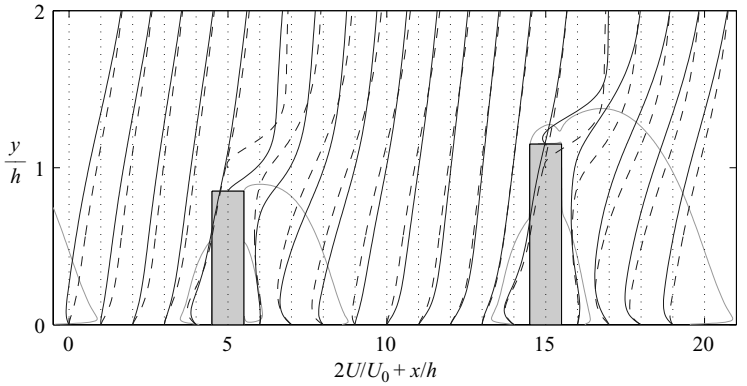

FIGURE 8. Rough-wall velocity profiles at various x locations, $x = 0$ to $19h$, for the uneven roughness case. Dashed lines denote the square rib case, F–1. Separation–reattachment regions are shown by light grey.

The uneven roughness case

Figure 8 shows $\overline{U}$ profiles in the roughness sublayer, $y < 2h$, for various x locations with zero-velocity contours, over one period of roughness geometry of the uneven roughness case. $\overline{U}$ is normalized by U_0, the maximum value for $y < 2h$. The velocity distribution of the even roughness case is also shown as a reference.

The primary reattachment length of the shorter rib is about $3.5h$, while that of the taller rib is about $5.5h$. Since the same rib separation is specified between each pair of ribs, the smaller recirculation bubble for the shorter rib provides a longer distance to form a fuller velocity profile. This increases the mass flux upstream of the taller rib within the roughness sublayer, and, therefore, explains why the pressure drag acting on a taller rib is about 42% larger than that on a square rib in Case F–1, with only a 15 % increase in rib height. For instance, the mass flux for $y \leqslant 2h$ at the middle of the upstream region for the taller rib, $x = 10h$ in figure 8, is about 1.5 times as large as that for the shorter rib at $x = 0$. If we assume that the same drag coefficient can be applied to both the ribs using these mass fluxes, or U velocity averages, we can estimate that the form drag acting on the taller rib would be about 2.8 times as large as that on the shorter. This is close to the factor 2.6 computed from the pressure distribution.

4.3. *Momentum budget*

The streamwise-averaged $\overline{U}$ equation for a rib-roughened channel can be written as

$$0 = -\left\langle \frac{\partial \overline{P}}{\partial x} \right\rangle - \frac{\partial}{\partial y}\left(\langle \overline{U}'\overline{V}' \rangle + \langle \overline{uv} \rangle - \nu \frac{\partial \langle \overline{U} \rangle}{\partial y} \right). \tag{4.2}$$

Unlike a uniform smooth-wall channel or pipe flow, the pressure term in (4.2) is not independent of y within roughness, since $\langle \partial_x \overline{P} \rangle = \partial_x \langle \overline{P} \rangle - \delta \overline{P}/\tilde{L}_x$, where $\partial_x \langle \overline{P} \rangle$ is the prescribed constant gradient, $\delta \overline{P}$ is the discontinuous change of pressure across rib roughness, and $\tilde{L}_x$ is the total field length of the fluid, the residue of L_x from which the total width of roughness elements is subtracted. This is recognized commonly along with the space-averaging procedure in a meteorological framework (Wilson & Shaw 1977; Raupach & Shaw 1982; Finnigan 2000). Although $\delta \overline{P}$ vanishes above roughness, it becomes a dominant term within wall roughness. This pressure effect is a notable property in the momentum balance for rough-wall turbulence.

Figure 9 shows the momentum budget of (4.2), normalized by the rough-wall friction velocity, for the rib-roughened channel. Within the roughness, Reynolds stress is the

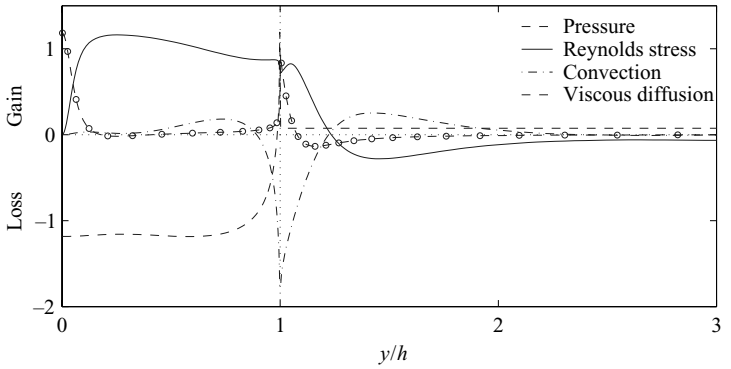

FIGURE 9. Momentum budget near the rough wall for square rib roughness, Case F–1. The budget is normalized by $u_{\tau_R}^2/h$. Reynolds stress and convection denote $-\partial_y\langle\overline{uv}\rangle$ and $-\partial_y\langle\overline{U}'\overline{V}'\rangle(=-\langle\partial_y\overline{U}\,\overline{V}\rangle)$, respectively.

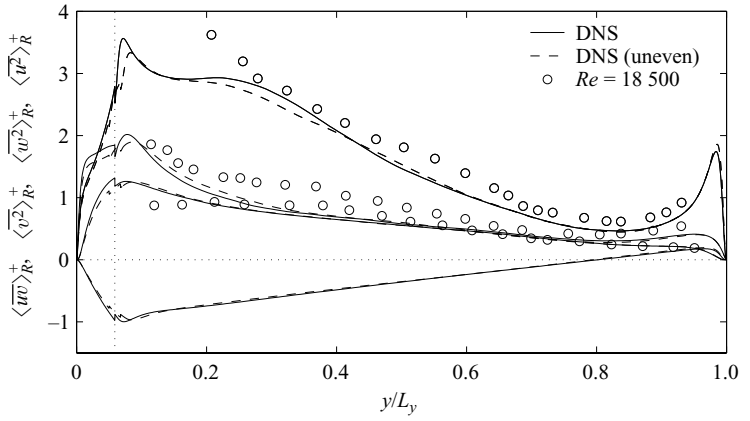

FIGURE 10. Streamwise-averaged Reynolds-stress distributions for the DNS cases and H–L.

other dominant term to balance the pressure term, except for the near-wall regions at the bottom and top of the roughness elements. Close to the bottom surface, the viscous term rises and balances pressure drag, because Reynolds stress vanishes on the wall. Since the pressure drag contributes adversely in the momentum budget, the viscous diffusion becomes positive at the surface, which makes the mean velocity gradient negative on the surface; it expresses the recirculation of mean flow. Near the top of roughness, dispersive momentum flux becomes significant as well, since the mean flow field provides large fluctuation from the streamwise average because of separation and recirculation near the roughness element. The dispersive term vanishes above $y \simeq 2h$, where the velocity profile regains the log-law. On the other hand, the observation by Ashrafian & Andersson (2003) on the momentum fluxes near a rib-roughened wall shows that the dispersive term could be significant over several roughness heights, while the roughness height in their simulation is relatively low, 13.6 wall units.

4.4. *Reynolds stress distributions*

Reynolds-stress distributions are shown for Cases F–1, M–2 and H–L in figure 10, normalized by the rough-wall friction velocity of each case. Throughout the channel, $\langle\overline{u^2}\rangle > \langle\overline{w^2}\rangle > \langle\overline{v^2}\rangle$ except close to the bottom of the rib elements, where $\langle\overline{u^2}\rangle < \langle\overline{w^2}\rangle$,

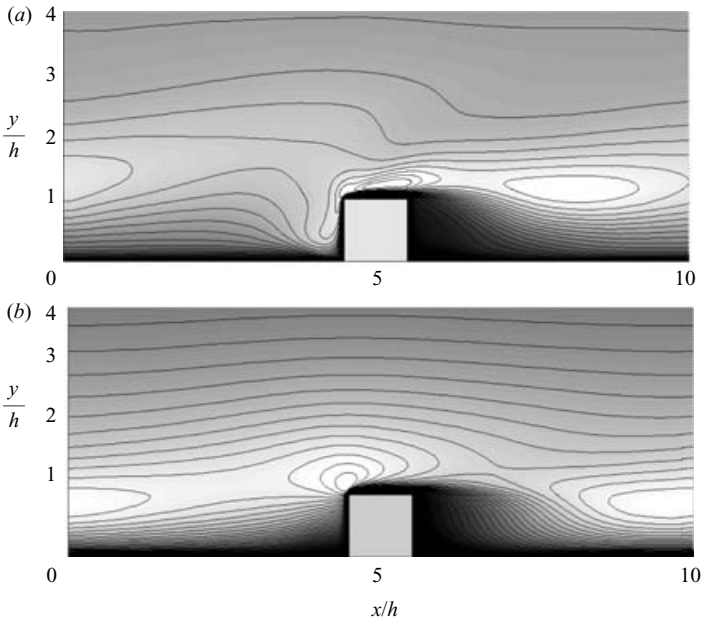

FIGURE 11. The turbulent kinetic energy distributions near the square rib for: (*a*) DNS (F–1); (*b*) RANS ($\overline{v^2}$–f). One contour level denotes 0.2 and grey-scales range between 0.2 (black) and 3.7 (white) wall units, normalized by $u_{\tau_R}^2$, respectively.

because two-dimensional transverse roughness prevents the streamwise velocity fluctuation, which intensifies the spanwise turbulent motions. The region near the smooth wall exhibits more intensive anisotropy than the rough-wall region, as will be discussed in § 6. A sharp peak of $\overline{u^2}$ at $y^+ \simeq 15$, which is effected by a smooth wall that has high viscous impedance, is not seen on the rough-wall side. In the middle of channel, $\langle\overline{w^2}\rangle \simeq \langle\overline{v^2}\rangle$. The maximum turbulent kinetic energy obtained from these streamwise-averaged values, $k_R^+|_{max} = \frac{1}{2}\langle\overline{u^2} + \overline{v^2} + \overline{w^2}\rangle|_{max}/u_{\tau_R}^2$, is 3.4, while the maximum on the smooth-wall side is 4.3 wall units, normalized using the smooth-wall friction velocity u_{τ_S}.

Although the tendency of the three components of TKE in H–L are replicated well in the numerical simulations, there is a certain amount of inconsistency, especially in the $\langle\overline{u^2}\rangle$ profiles near the rough wall. The laboratory results of other Reynolds numbers present no discernible variations, if normalized by the rough-wall friction velocity, over the range from it $\mathrm{Re} = 18\,500$ to $56\,000$, based on the maximum velocity and channel half-width. A possible reason for this inconsistency between both the studies is the low-Reynolds-number effect in our DNS case.

As can be seen from the streamwise-averaged Reynolds-stress distributions in figure 10, TKE has its maximum just above the rib roughness, averaged in the streamwise direction. Figure 11 compares the TKE distributions between DNS and RANS around square-rib roughness. Maximum TKE regions are observed just above the rib. Boundary-layer separation which occurs on the bluff body produces non-periodic spanwise vortex shedding. It leads to a high turbulent energy area, especially for $\overline{u^2}$, in the downstream region. Comparing the DNS and RANS cases, the two-dimensional distributions are rather different.

The DNS result shows that TKE has a peak over the rib top-face, and that the high energy is convected downstream with the mean flow. In the RANS k solution,

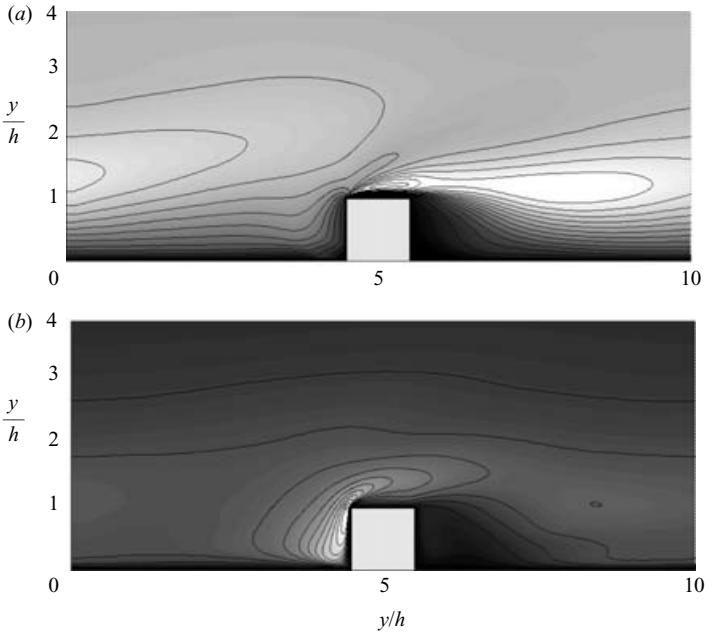

FIGURE 12. The distributions of turbulent intensities normalized by u_{τ_R}. (*a*) $\overline{u^2+v^2}$; (*b*) $\overline{w^2}$. One contour level indicates 0.4 and grey-scales ranges between 0 (black) and 2.7 (white) wall units, normalized by $u_{\tau_R}^2$, respectively.

the peak comes close to the upstream face corner, at which the positive definite TKE production term, computed using the eddy viscosity, reaches its maximum, since the magnitude of the mean velocity strain increases at the corner. On the contrary, the TKE production term of the DNS case includes a negative region near the corner.

In addition, a secondary high-energy region exists upstream of the rib in figure 11(*a*), which is not replicated by RANS. Since the flow is blocked in the streamwise direction by strip roughness, the spanwise velocity fluctuation is intensified, as seen in the streamwise-averaged Reynolds-stress distributions (figure 10). If we examine the vortices of the wall-normal direction, the unsteady motions of ω_y vortical structure are observed, generated near the upstream side of the rib (figure 15). This is another notable aspect of the TKE generation for strip roughness, which cannot be reproduced by steady-state two-dimensional RANS.

The difference in the high-kinetic-energy regions can be understood by inspecting each component of Reynolds stress. Figure 12 shows the two-dimensional distributions of $\overline{u^2+v^2}$ and $\overline{w^2}$. The $\overline{u^2+v^2}$ distribution indicates that the x–y unsteady motions largely account for the high-energy region just above and downstream of the rib roughness. On the other hand, $\overline{w^2}$ clearly shows its maximum on the upstream face of the rib. Both the maximum values are almost of the same order: $\overline{u^2+v^2}_R^+|_{max} = 6.1$, $\overline{w^2}_R^+|_{max} = 5.6$.

5. Vortical structure

5.1. *Instantaneous view*

The vortical structure is important in both production and dissipation of turbulent kinetic energy. Whereas an energetic range of vorticity produces energy through

FIGURE 13. Iso-surfaces of ω_x near the smooth wall. Dark grey, +25.0%; light grey, −25.0% of $|\omega_x|_{S_{max}}$, respectively, or ± 0.37 wall units, normalized by $u_{\tau_S}^2/\nu$.

FIGURE 14. Iso-surfaces of ω_x near the rough wall. Dark grey, +5.0%; light grey, −5.0% of $|\omega_x|_{R_{max}}$, respectively, or ± 0.19 wall units, normalized by $u_{\tau_R}^2/\nu$.

vortex shedding and stretching, a dissipative range with the Kolmogoroff length scale accounts for the energy dissipation. Here, the instantaneous three-dimensional vortical structures are compared in the neighbourhood of the smooth- and rough-wall through visualization. A notable dynamical change of turbulence structure can be seen in the instantaneous near-wall vorticity field, as also seen in the averaged results that will be shown in § 5.2. Figures 13 and 14 show the iso-surfaces of streamwise vorticity field near the smooth and rough walls, for $\omega_x = \pm 0.25\,|\omega_x|_{S_{max}}$ and $\omega_x = \pm 0.05\,|\omega_x|_{R_{max}}$, respectively, where $|\omega_x|_{S_{max}}$ and $|\omega_x|_{R_{max}}$ are the maximum values given in each field shown.

On the smooth-wall side, the vortical streaks are clearly captured, elongated in the streamwise direction. They serve as an energy source in the non-equilibrium layer and account for the near-wall behaviour of TKE. The development of these near-wall streaks in vorticity and velocity fluctuation was studied by Butler & Farrell (1992) through the Orr–Sommerfeld eigenmode analysis. On the other side of the channel (figure 14), the transversely mounted rib roughness disrupts the ω_x streaks in the roughness sublayer. The disturbed streaks form a high ω_x fluctuating region downstream of each rib; it corresponds to the intensive TKE dissipation. Since neither $\overline{v^2}$ or $\overline{w^2}$ becomes significant in this region, these high ω_x streaks lie mostly within the dissipative vorticity range. Not very coherent vortical structures are observed; rather complex patterns of vorticity iso-surfaces, primarily formed above and downstream of the rib, are visualized in the figure. This suggests that regular periodically mounted strip roughness produces irregular complicated turbulent motions near the wall.

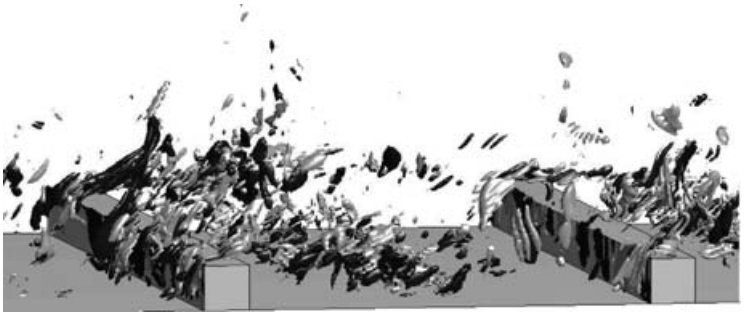

FIGURE 15. Iso-surfaces of ω_y near the rough wall. Dark grey, +5.0%, light grey, −5.0%; of $|\omega_y|_{R_{max}}$, respectively, or ± 0.21 in wall units, normalized by $u_{\tau_R}^2/\nu$.

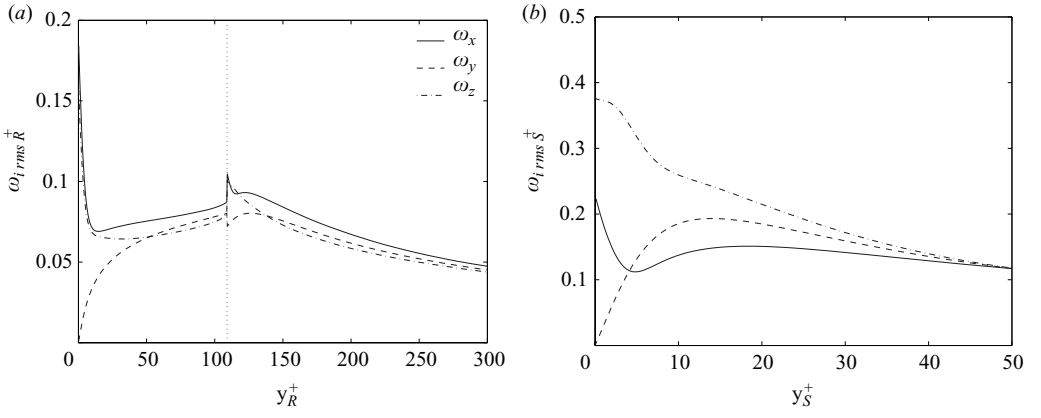

FIGURE 16. Near-wall distributions of $\omega_{i\,rms}$ in wall units. (*a*) Rough-wall distributions, normalized by $u_{\tau_R}^2/\nu$. (*b*) Smooth-wall distributions, normalized by $u_{\tau_S}^2/\nu$.

Two-dimensional roughness produces three-dimensional, incoherent vorticity, mimicking the effect of sand-grain roughness; this is the origin of *k*-type roughness in a microscopic view.

The deflection of vortical streaks can be understood better by examining ω_y around the roughness elements; figure 15 shows the iso-surfaces for $\omega_y = \pm 0.05|\omega_y|_{R_{max}}$. The vortical streaks from the upstream region are deflected by the rib roughness, and attached on the upstream side of each roughness element. Then, these wall-normal vortices break down in the downstream region as they merge into the irregular vortex-shedding motions. These disrupted vortical structures near rib-roughened wall were also reproduced numerically by Leonardi *et al.* (2003*a*) and Nagano *et al.* (2004), and agree well with their observations.

As the TKE distribution has a peak due to the *w*-fluctuation near the upstream face of each rib, these ω_y streaks have a crucial effect on the $\overline{w^2}$ production. The vortices attached on the rib are intensified by vortex stretching because of the high strain at the upstream corner. This vortical motion produces the spanwise velocity fluctuation near the rib front, combined with blocking of two-dimensional mean flow by transversely placed rib roughness.

5.2. *Averaged result*

The near-wall vortical structures are explained by examining averaged profiles. Figure 16 shows near-wall distributions of r.m.s. vorticity fluctuations normalized

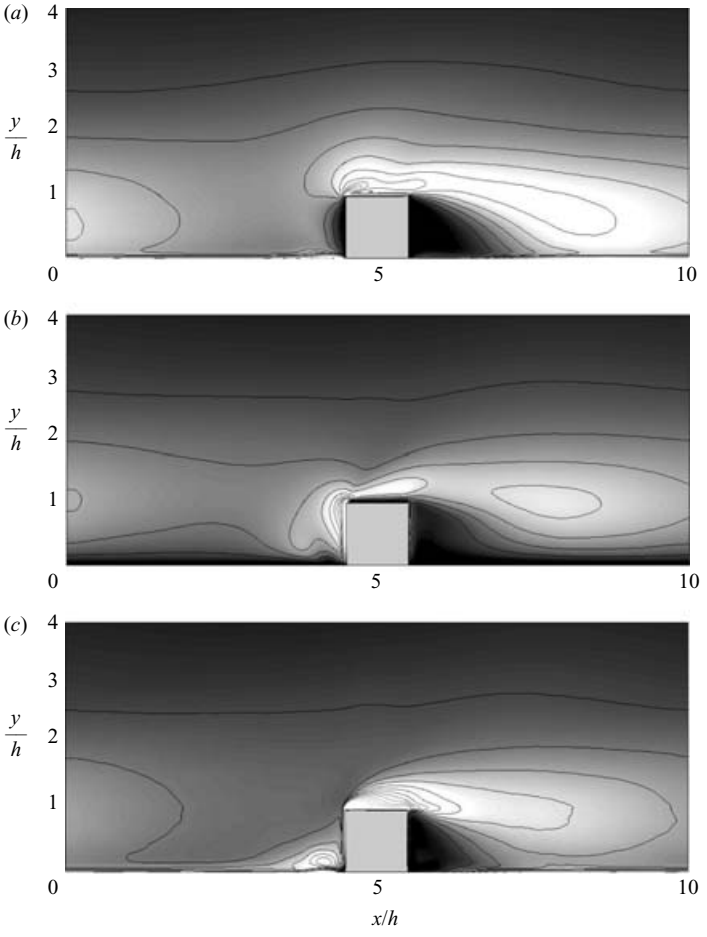

FIGURE 17. The two-dimensional distributions of r.m.s. values of vorticity near rib roughness for: (*a*) $\omega_{x\,rms}$; (*b*) $\omega_{y\,rms}$; (*c*) $\omega_{z\,rms}$. One contour level denotes 0.015 and grey-scales range between 0.025 (black) and 0.1 (white) wall units, nomalized by $u_{\tau_R}^2/\nu$, respectively.

by the friction velocities on each wall. Toward the middle of the channel, the vorticity fluctuations of all three directions collapse. In this high-Reynolds-number region, dissipative behaviour is supposed to be dominant in r.m.s. vorticity; therefore, dissipation is isotropic in the channel. Anisotropy arises near both ends of the channel owing to the wall effects. The smooth-wall vorticity distributions are similar to those obtained in other DNS studies with a smooth wall (e.g. Kim, Moin & Moser 1987). The local minimum of $\omega_{x\,rms}$ implies the presence of streamwise vortices peculiar to the smooth wall. In the rough-wall vorticity distributions, all three components collapse within a close range above the roughness. Within the roughness, ω_x and ω_z show similar profiles from the bottom surface to the rib top, although two-dimensional views reveal different distributions. The value of ω_y drops towards 0 reaching the bottom, as the smooth wall.

In figure 17, the two-dimensional distributions of r.m.s. vorticity fluctuations are compared in all three directions. The term $\omega_{x\,rms}$ has an intense region downstream of each rib roughness. This corresponds to a significant dissipation region in the TKE

budget. The dissipative region of $\omega_{x_{rms}}$ shows an intense region from the rib top to the downstream bottom. Within the roughness, the pressure redistribution term balances this dissipative region, rather than the production term. $\omega_{y_{rms}}$ has a peak region attached on the upstream side of the rib. This region corresponds to a high $\overline{w^2}$ region shown in figure 12(*b*). Wall-normal vorticity streaks produce the spanwise velocity fluctuation. $\omega_{z_{rms}}$ shows peaks not only just above the rib, but also in the recirculation region of the upstream side of the rib. As will be shown in the following section, ω_z is produced by unsteady non-periodic vortex shedding; the large-scale motions are those most responsible in the $\overline{u^2}$ production.

5.3. *Vortex evolution in the roughness sublayer*

Here, the spanwise structure of vorticity fields in the roughness sublayer is discussed by visualization of a time-dependent solution. As shown in figure 9, since the turbulent shear stress is the dominant term in the roughness sublayer to balance the pressure drag, strong mixing occurs within and above the roughness to produce the turbulent shear. It induces the intensive mass and momentum exchange between the wall layer and bulk flow. This flow structure is primarily caused by the unsteady eddies formed near the roughness element. The presence of the unsteady vortices distinguishes *k*-type and *d*-type roughnesses, as mentioned in § 1. Direct numerical simulation is able to follow the development and evolution of this vortical structure through visualizations.

Figures 18 shows a time sequence of spanwise fluctuation vorticity ω_z, on a subset of an (x, y)-plane for $0 \leqslant x/h \leqslant 20$, $0 \leqslant y/h \leqslant 3$, over the period $t/t_h = 0$ to 7.7, where the simulation time is normalized by $t_h = h/U_{bulk}$. Because of the mesh-stretch effect, weak unsteady oscillatory behaviour is seen in the mesh-expanding region downstream of the rib. However, it has been confirmed that this numerical error has been significantly reduced from the solution on a coarser grid used in the grid independence study. In figure 18, the development of spanwise vortices near rib roughness is captured; these vortices are formed through the interaction of the bulk flow and roughness elements. For example, in figure 18(*b*), a vortex formed downstream of the left rib can be recognized, produced by the mixing of mean flow and relatively slow inner flow behind the rib. In the same figure, a vortex that represents upstream recirculation is developing ahead of the right rib. This produces a high $\omega_{z_{rms}}$ region at the upstream lower corner shown in figure 17. However, these vortices are very unstable and shed into the outer layer shortly after the development, since they are not confined in the cavity, unlike *d*-type roughness as shown by Perry *et al.* (1969). In figures, 18(*c*) and 18(*d*), the vortices are deformed and merged into smaller elongated eddies; in figure 18(*e*), no apparent vortex configuration can be found.

As mentioned in § 1, the LES study by Shah & Ferziger (1998) showed the presence of horseshoe-vortex shedding around a cube mounted on a wall. This is an example of coherent motions for the flow over a three-dimensional obstacle. However, our time sequences of vortical structures presented above are irregular and complicated compared to their result, as generated on two-dimensional geometry.

On the other hand, in a meteorological framework, a mixing-layer analogy has been suggested for a two-dimensional organized structure in the roughness sublayer (Raupach, Finnigan & Brunet 1996; Finnigan 2000). Originally, the mixing layer refers to a turbulent mixing motion produced by the interaction of two uniform non-turbulent flows. However, they proposed an analogy between a coherent structure in a fully turbulent canopy flow and a plane mixing layer. A two-dimensional mechanism for the mixing-layer development, which is caused by the Kelvin-Helmholtz instability,

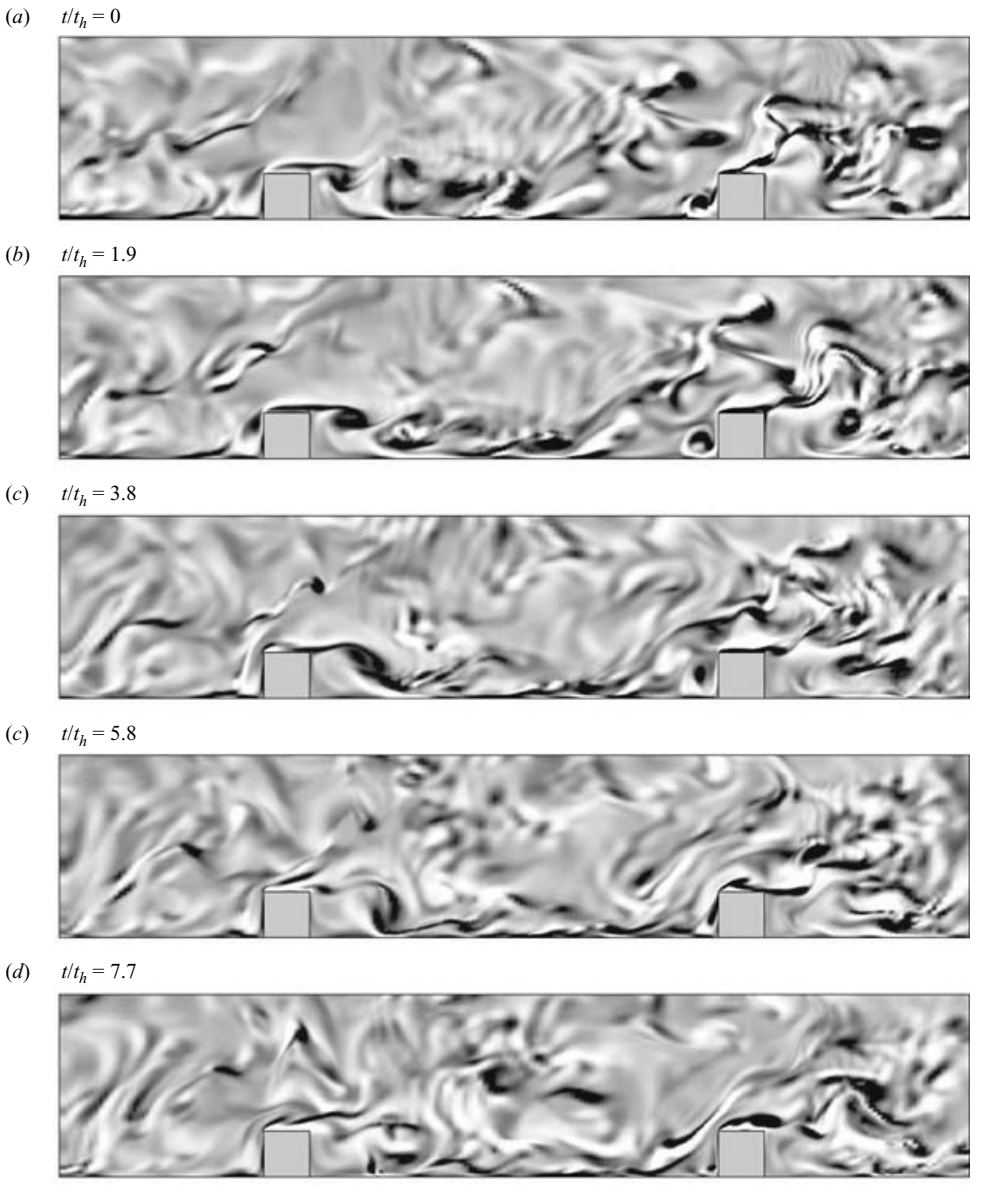

FIGURE 18. Time sequence of spanwise vorticity ω_z ($-0.1 < \omega_z^+{}_R < 0.1$) near rib roughness in an (x, y)-plane. Simulation time is normalized by $t_h = h/U_{bulk}$.

has also been suggested. Other atmospheric and laboratory studies also support the occurrence of a plane-mixing-layer structure (Zhuang & Wilson 1994; Judd, Raupach & Finnigan 1996; Brunet & Irvine 2000; Novak *et al.* 2000; Poggi *et al.* 2004*a*, *b*). Mixing-layer-type coherent vortical motions are supposed to develop near the roughness top in a canopy flow, although the applicability of this analogy to general *k*-type roughness is unclear. However, our visualization presents no obvious coherence sustained over the time-dependent ω_z field. Only unsteady transient vortices are produced near the roughness elements, which intensifies the mixing mechanism in the roughness sublayer.

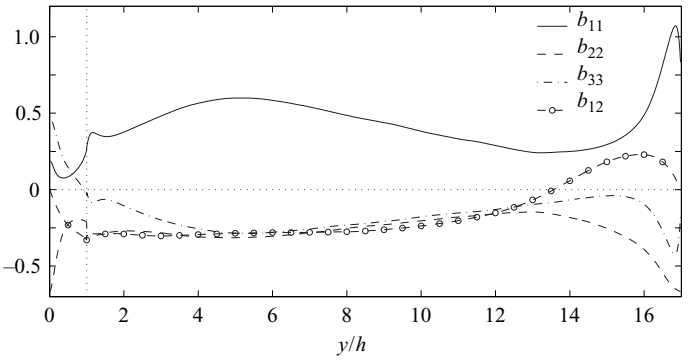

FIGURE 19. Streamwise-averaged Reynolds stress anisotropy tensor distributions. $b_{ij} = \overline{u_i u_j}/k - (2/3)\delta_{ij}$.

6. Near-wall anisotropy

In the literature on rough-wall turbulence, anisotropy in a rough-wall boundary layer is often of interest. Correlations and spectra of velocity or vorticity have been experimentally measured and compared to the isotropic relations. Here, we examine the variation of near-wall anisotropy through single-point correlations in our DNS case.

The Reynolds-stress anisotropy tensor

$$b_{ij} = \frac{\overline{u_i u_j}}{k} - \tfrac{2}{3}\delta_{ij}, \tag{6.1}$$

provides a measurement of isotropy in terms of Reynolds stress. The diagonal components, b_{11}, b_{22}, b_{33} of the anisotropy tensor lie between $-2/3$ and $4/3$; the trace $b_{ii} \equiv 0$ is an invariant of b_{ij}. The streamwise average of b_{ij} in Case F–1 is shown in figure 19. As can be seen from the b_{11} distribution, and also can be inferred from the Reynolds stress distributions in figure 10, strong anisotropy arises in b_{11} through the near-wall behaviour of $\overline{u^2}$ on the smooth-wall side. However, on the rough-wall side, anisotropy is considerably reduced. Just above the roughness, and also below the b_{11} maximum on the smooth-wall side at $y \simeq 14$, b_{11} reaches its local maxima, while b_{33} comes close to zero. Towards the middle of channel, anisotropy is gradually reformed, as $b_{11} > 0$, and $b_{22} \approx b_{33}$.

Near-wall anisotropy can also be examined using a dissipative small-scale of turbulence structure. The ratios of variances of velocity derivative and vorticity have been studied as a measure of isotropy of dissipation in various flows (Browne, Antonia & Shah 1987; Shafi & Antonia 1997). Shafi & Antonia (1997) measured the following parameters for a boundary-layer flow over mesh roughness:

$$\left.\begin{aligned} K_1 &\equiv 2\,\overline{(\partial_x u)^2}\,/\,\overline{(\partial_x v)^2}, \\ K_2 &\equiv 2\,\overline{(\partial_x u)^2}\,/\,\overline{(\partial_x w)^2}, \\ K_3 &\equiv 2\,\overline{(\partial_x u)^2}\,/\,\overline{(\partial_y u)^2}, \\ K_4 &\equiv 2\,\overline{(\partial_x u)^2}\,/\,\overline{(\partial_z u)^2}, \\ K_{\omega_2} &\equiv 5\,\overline{(\partial_x u)^2}\,/\,\overline{\omega_y^2}, \\ K_{\omega_3} &\equiv 5\,\overline{(\partial_x u)^2}\,/\,\overline{\omega_z^2}. \end{aligned}\right\} \tag{6.2}$$

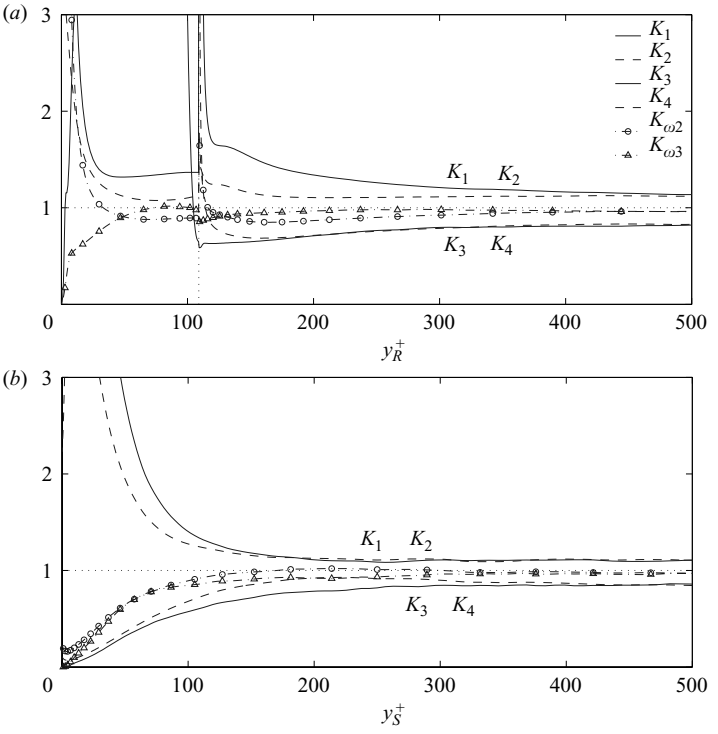

FIGURE 20. Distributions of the ratios, (6.2): (*a*) near the rough wall; (*b*) near the smooth wall.

In isotropic turbulence, the above ratios are all equal to 1. We examine the isotropy for the rib-roughened channel flow using these parameters.

Figure 20 shows the parameters in (6.2) near the rough and smooth walls. Some parameters have singularity at the solid surface, although near-wall behaviour of each parameter can be distinguished. Away from the wall, $K_1 \simeq K_2 > 1$ and $K_3 \simeq K_4 < 1$ are the limiting relations in the middle of the channel. It agrees with the cases reviewed by Browne *et al.* (1987); they summarized these ratios for various flows. In our DNS case, approximately $K_1 = K_2 = 1.1$ and $K_3 = K_4 = 0.8$ in the middle of the channel. Also, $K_{\omega_2} \simeq K_{\omega_3}$ since $\overline{\omega_y^2}$ and $\overline{\omega_z^2}$ collapse away from the wall, as in figure 16; they are closer to 1 than the other ratios. Comparing between the smooth- and rough-wall values, a shorter relaxation distance is observed in the rough-wall case to reach the limiting state. Above the rough wall, all the ratios quickly approach the limiting values. Within the roughness, all the ratios except K_3 reach a settled state at $y_R^+ \simeq 50$. The relaxation in the smooth-wall case is rather slow. The reduction of anisotropy on a rough wall is also observed in dissipative length scales.

The above observation on the reduction of anisotropy is primarily due to the difference in turbulence structure near wall, as seen in the instantaneous flow visualization in § 5. The coherence in vortical structure near a smooth wall prevents the flow from reaching isotropy. However, the rough-wall disrupted vortices lose this anisotropic structure and alters the characteristic length-scales near wall. This was also confirmed both experimentally and numerically (e.g. Krogstad & Antonia 1994; Leonardi *et al.* 2003*a*) through the examination of two-point correlations for *k*-type roughness.

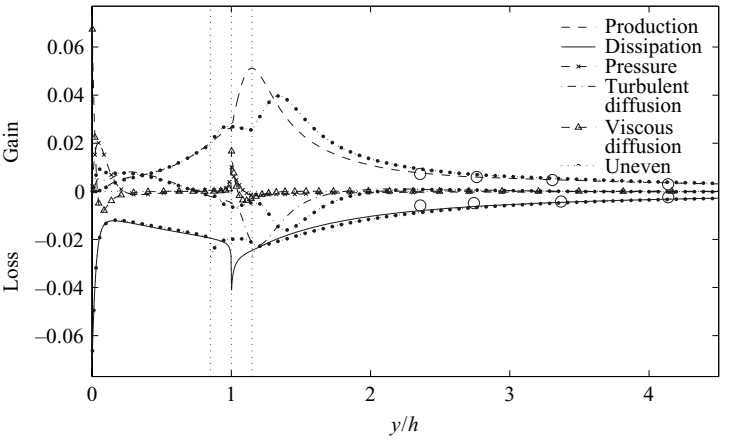

FIGURE 21. Turbulent kinetic energy budget near the rough wall, normalized by $u_{\tau_R}^4/\nu$: ○, H–L ($Re = 18\,500$).

7. TKE budget and wall-normal flux

To compute the turbulence statistics, the sampling is done at the staggered mesh locations for the Reynolds stress budgets of the $\overline{u^2}$, $\overline{v^2}$ and $\overline{w^2}$ transport equations. The same second-order discretizations as those employed in the governing equations are used for all terms in these equations. Then, each obtained statistical term is summed up at the middle of the numerical cell for turbulent kinetic energy.

7.1. *TKE budget*

The streamwise-averaged, TKE transport equation can be written as follows:

$$\left\langle \overline{U}_j \frac{\partial k}{\partial x_j} \right\rangle = \langle \mathscr{P} \rangle - \langle \varepsilon \rangle - \frac{\partial \langle \overline{pv} \rangle}{\partial y} - \frac{1}{2} \frac{\partial \langle \overline{u_k u_k v} \rangle}{\partial y} + \nu \frac{\partial^2}{\partial y^2} \langle k \rangle, \tag{7.1}$$

where $\mathscr{P}$ is the TKE production term, $-\overline{u_i u_j} \partial_j \overline{U_i}$; ε is the TKE dissipation term, $\nu \, \overline{\partial_j u_i \partial_j u_i}$. Figure 21 shows the distributions of each term in (7.1) near the rough wall. The convection term, the left-hand side in (7.1), is omitted since its contribution has been found to be small except in the vicinity of $y = h$. Production and dissipation terms from H–L are also shown, although only the measurements far from the roughness elements are provided. The budgets on the smooth-wall side are similar to those of smooth-wall channel flows (Moser, Kim & Mansour 1999), although our results show that the high-Reynolds-number limit is not achieved; they are not presented here.

As can be seen from the TKE budget, strong energy production is observed just above the roughness. Such a near-wall production peak can also be seen in smooth-wall turbulence; for a channel flow with a sufficiently high Reynolds number, $\overline{uv}^+ = 1/2$ gives the maximum $\mathscr{P}^+ = 1/4$, which occurs where viscous stress equals the Reynolds stress. On the rough side, the viscous sublayer is disrupted. Irregular vortical motions, induced by separation at roughness elements, produce high turbulence intensities, which results in a high production region, as described in § 4.4. The difference of production and dissipation is balanced by turbulent diffusion, so that a sharp peak of energy production develops, with energy fluxes both toward the outer layer and into the roughness elements.

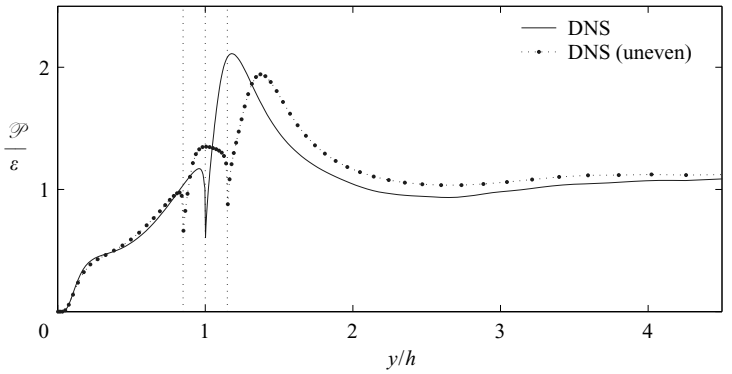

FIGURE 22. The ratio of the TKE production term to the TKE dissipation term for even and uneven roughnesses.

Further from the wall, the turbulent diffusion term reaches zero by $y \simeq 2h$; above this location, production and dissipation balance so that an equilibrium outer layer is established. The flow in this layer obeys a logarithmic law, which is confirmed by the velocity profile in figure 5. Figure 22 shows the ratio of the production term to the dissipation. The above observation on equilibrium is also confirmed by this ratio; above $y \simeq 2h$, $\mathscr{P}/\varepsilon$ becomes close to 1.

On the contrary, below $y \simeq 2h$, the flow is directly, dynamically influenced by the roughness. The dispersive effects arise because of the non-uniform distribution of mean quantities in the streamwise direction. The direct influence by roughness is observed not only in the TKE budget, but also in the velocity profile (figure 6). The deviation of the mean U profile from the log-profile is insignificant above $y > 2h$ throughout the channel. This inner region can be identified as the roughness sublayer. We can assume that the layer width in our DNS case is about $2h$; above that, an equilibrium log-layer is established, regardless of the roughness geometry. The TKE budgets obtained in the DNS studies by Miyake *et al.* (2001) and Nagano *et al.* (2004) also show that the flow reaches an equilibrium state at $y \simeq 2h$ for a rib-roughened wall channel flow, although their roughness heights were relatively low. Raupach *et al.* (1991) suggest $2h$–$5h$ for roughness sublayer width in general cases.

Within the roughness, the behaviour of smooth wall turbulence is replicated for dissipation and viscous diffusion near the bottom of the roughness element; these two terms have peaks on the bottom surface to balance. On the other hand, production is rather sluggish at $y_R^+ \approx 10$, where it would be maximum for smooth-wall turbulence. The pressure term becomes more significant in this region. It serves as an energy source near the strip roughness bottom; further from the bottom, close to the top, the pressure term reaches zero, except for a small oscillation in the vicinity of rib top face. The production term slowly increases toward the energy source area above the rib roughness. Zhuang & Wilson (1994) estimated that pressure redistribution would show a significant amount of loss in the TKE budget for a forest canopy flow near the canopy top. However, the result of our case does not support their observation.

Figures 21 and 22 also contain the results of uneven roughness, Case M–2. In the TKE budget, the production, dissipation, and turbulent diffusion terms are included. Since the top solid face of rib roughness causes a discontinuous peak in statistics, uneven roughness relaxes this peak by employing two different heights. Each term agrees with the result of the square rib height in Case F–1 below the shorter rib height

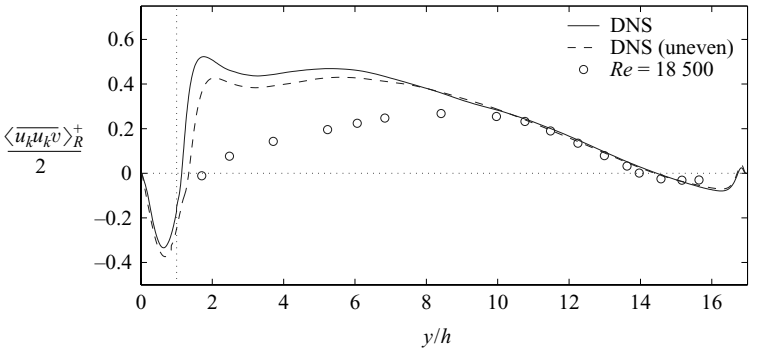

FIGURE 23. Turbulent kinetic energy flux in the wall-normal direction: ○, H–L ($Re = 18\,500$), normalized by $u_{\tau_R}^3$.

in Case M–2. However, the peaks of production and turbulent diffusion, located above the roughness, are shifted further from the wall, as those peak values are reduced. The peak location is determined by the taller roughness; the shorter shows less significant effects. This is another instance of the dominance of taller roughness in TKE production.

7.2. *TKE flux*

Figure 23 shows the streamwise average of turbulent kinetic energy flux in the wall-normal direction throughout the channel for Cases F–1 and M–2; the experimental data of H–L are also shown. The profiles of the DNS cases and the experiments collapse above $y \approx 10h$, but show a significant difference near the rough wall. As pointed out by Raupach *et al.* (1991), measurements within or close to roughness have experimental difficulties, especially for higher-order correlations. Therefore, these measurements of triple velocity correlations may not be precise in the intensive turbulence region, i.e. near the roughness elements.

As seen from the TKE budget in figure 21, there is a strong energy source just above the roughness element. It produces the energy fluxes in both the upward and downward directions; zero-TKE flux is found at just above the roughness. In $y < h$, a negative flux, formed within the roughness, diffuses the kinetic energy into the rough surface. In the equilibrium layer above $y \approx 2h$, the flux reaches its positive maximum and becomes almost constant up to $y \approx 6h$, and then gradually reduces to balance the energy flux from the smooth-wall side. On the smooth-wall side, zero-TKE flux is observed in the maximum production region, at $y_S^+ \approx 15$; maximum TKE flux is then achieved at $y_S^+ \approx 40$ where a logarithmic layer begins to form. Although the turbulence structures that give the maximum production are different, the streamwise average of the TKE fluxes has a similar dependence on the production term.

For the uneven roughness, the location of zero-TKE flux is shifted upward, as is the production peak. However, the lower grid resolution in Case M–2 causes a discrepancy of the maximum and minimum values of flux; this discrepancy is also seen in our preliminary coarse-grid solutions. The difference between even and uneven roughnesses on TKE flux is unclear, other than shifting the position of zero flux.

Figure 24 shows the two-dimensional distribution of $\overline{u_k u_k v}/2$ around the rib roughness. Strong negative fluxes are formed on the upstream and upper sides of the rib, and in the downstream region. Clearly, the high TKE regions correspond to the source of TKE flux. The contour lines are densely distributed; those regions

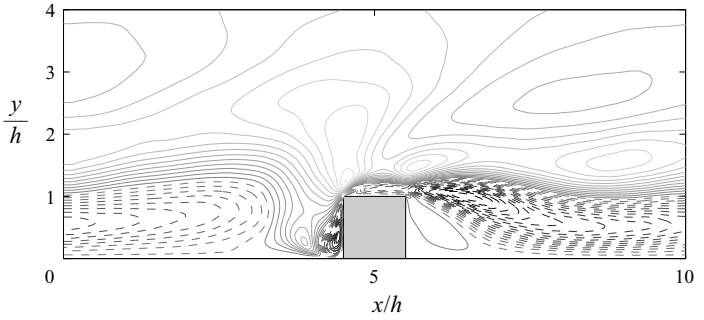

FIGURE 24. Turbulent kinetic energy flux in the wall-normal direction, $\overline{u_k u_k v}/2$. One contour level indicates 0.06 wall units, normalized by $u_{\tau_R}^3$. The dashed line denotes negative values.

are highly non-equilibrium. There are two regions that have positive TKE fluxes within the roughness, $y < h$. Both are caused by mean flow recirculation around the rib. Distinctively, on the upstream side of the rib, the recirculation produces a high positive flux region, which results a high $\overline{w^2}$ region; hence, it produces a significant positive TKE flux in the wall-normal direction by the contribution from the flux $\overline{w^2 v}$.

8. Summary and conclusion

Direct numerical simulations were conducted for the flow in a rib-roughened asymmetric channel. Sufficiently resolved detailed statistical and instantaneous data were computed and visualized. Three-dimensional visualizations of instantaneous fields provided insight into flow structures near a rough wall, as well as ensemble-averaged data.

Conventionally, a rough-wall boundary layer had been dealt with by using an *a priori* assumption: regardless of near-wall flow structure, a logarithmic law is universally valid at a sufficiently high Reynolds number for any type of wall. It prevails well above the surface, after adjusting the additive constant. The validity of this modified log-law has been attested by many experimental studies. Here we also confirmed that a logarithmic layer exists above the roughness wall layer, through the velocity profile and TKE budget obtained in the simulations. Approximately above $y \simeq 2h$, an equilibrium layer is established, which follows a logarithmic velocity profile. The reformed additive constant for the fully rough state obtained in our velocity profile agrees with the experiment by Hanjalić & Launder (1972) and also corresponds to the result provided by Leonardi *et al.* (2003*b*).

As can be seen in both averaged and instantaneous results, a number of flow properties in the rough-wall vicinity show rather different behaviour from the smooth-wall side. For instance, aerodynamic drag is dominant in the wall shear forces on the rough surface, instead of viscous drag, as was seen in other numerical studies (e.g. Leonardi *et al.* 2003*b*). Although non-equilibrium regions are established within the wall-layer, or below the log-layer, of both smooth and rough walls, the flow structure on each wall is different, as shown in the visualizations. Transversely mounted rib roughness raises the disarrangement of vortical streaks in the streamwise and wall-normal directions, as well as inducing the non-periodic irregular spanwise vortex shedding, which serves as energy sources for the TKE flux towards the wall surface as well as into the bulk flow. These unsteady vortical motions are represented in the Reynolds shear stress within and above the roughness, which offsets the pressure

gradient in the channel and leads to the reproduction of a log-profile. It should also be remarked that the two-dimensional rib roughness, composed of smooth planes, produces three-dimensional unorganized motions of vortices that disturb the viscous sublayer, and bears a resemblance to sand-grain roughness; wall roughness enhances the three-dimensionality of flow structure, as well as reducing near-wall anisotropy. This is consistent with the observation in other numerical simulations (Ikeda & Durbin 2002; Ashrafian & Andersson 2003; Leonardi *et al.* 2003*a*; Nagano *et al.* 2004).

We have also tested a two-dimensional RANS approach in comparison with the DNS results obtained here. If we use a rough-wall model, which is calibrated for the displacement of a modified log-law, we can find agreement with experimental data, as was demonstrated by Durbin *et al.* (2001). However, when solved for the full geometry and averaged in x, the RANS models used here underestimate the form drag acting on rough-wall elements, and hence cannot correctly represent the modified log-law, even though they are consistent with the universal logarithmic law of a smooth-wall boundary layer. One way to explain this is that the roughness elements disrupt the equilibrium wall streaks, producing turbulence structure that is not consistent with the empiricism in the model.

Our DNS results show different turbulence structures between the smooth and ribbed walls: the long streaks observed near a smooth wall become highly irregular vortices. This may explain why the correct log-law displacement is not expected from a RANS when we grid around the roughness. Log-law displacement is not a RANS prediction, it is an empirical input to the model. Hence, models that are developed for smooth walls do not capture the effect of altered turbulence structure.

This research was sponsored by the Office of Naval Research, grant N00014-01-1-0419-P00003. Primary computer resources were provided by the U. S. Army Engineer Research and Development Center–Major Shared Resource Center (ERDC MSRC), the Army High Performance Computer Research Center (AHPCRC), and the Naval Oceanographic Office–Major Shared Resource Center (NAVO MSRC).

REFERENCES

Akselvoll, K. & Moin, P. 1995 Large eddy simulation of turbulent confined coannular jets and turbulent flow over a backward facing step. *Rep.* TF-63, Thermosciences Division, Dept. of Mechanical Engineering, Stanford University.

Arora, R., Kuo, K. K. & Razdan, M. K. 1982 Near-wall treatment for turbulent boudary-layer computations. *AIAA J.* **20**, 1481–1482.

Ashrafian, A. & Andersson, H. I. 2003 DNS of turbulent flow in a rod-roughened channel. In *Proc. Third Intl Symp. on Turbulence and Shear Flow Phenomena*, vol. 1, pp. 117–122. Sendai, Japan.

Bandyopadhyay, P. R. 1985 Rough-wall turbulent boundary layers in the transition regime. *J. Fluid Mech.* **180**, 231–266.

Browne, L. W. B., Antonia, R. A. & Shah, D. A. 1987 Turbulent energy dissipation in a wake. *J. Fluid Mech.* **179**, 307–326.

Brunet, Y. & Irvine, M. R. 2000 The control of coherent eddies in vegetation canopies: streamwise structure spacing, canopy shear scale and atmospheric stability. *Boundary-Layer Met.* **94**, 139–163.

Butler, K. M. & Farrell, B. F. 1992 Three-dimensional optimal perturbations in viscous shear flow. *Phys. Fluids* **4** (8), 1637–1650.

Cherukat, P., Na, Y., Hanratty, T. J. & McLaughlin, J. B. 1998 Direct numerical simulation of a fully developed turbulent flow over a wavy wall. *Theoret. Comput. Fluid Dyn.* **11**, 109–134.

Cui, J., Patel, V. C. & Lin, C.-L. 2003 Large-eddy simulation of turbulent flow in a channel with rib roughness. *Intl J. Heat Fluid Flow* **24**, 372–388.

De Angelis, V., Lombardi, P. & Banerjee, S. 1997 Direct numerical simulation of turbulent flow over a wavy wall. *Phys. Fluids* **9**, 2429–2442.

Djenidi, L., Elavarasan, R. & Antonia, R. A. 1999 The turbulent boundary layer over transverse square cavities. *J. Fluid Mech.* **395**, 271–294.

Durbin, P. A. 1991 Near-wall turbulence closure modeling without 'damping functions'. *Theoret. Comput. Fluid Dyn.* **3**, 1–13.

Durbin, P. A. 1995 Separated flow computations with the k–ε–v^2 model. *AIAA J.* **33**, 659–664.

Durbin, P. A., Medic, G., Seo, J.-M., Song, S. & Eaton, J. K. 2001 Rough wall modification of two-layer k–ε. *Trans. ASME* I: *J. Fluids Engng* **123**, 16–21.

Finnigan, J. 2000 Turbulence in plant canopies. *Annu. Rev. Fluid Mech.* **32**, 519–571.

Hanjalić, K. & Launder, B. E. 1972 Fully developed asymmetric flow in a plane channel. *J. Fluid Mech.* **51**, 301–335.

Ikeda, T. & Durbin, P. A. 2002 Direct simulations of a rough-wall channel flow. *Rep.* TF-81, Flow Physics and Computation Division, Dept. of Mechanical Engineering, Stanford University.

Ikeda, T. & Durbin, P. A. 2004 Mesh stretch effects on convection in flow simulations. *J. Comput. Phys.* **123**, 110–125.

Jackson, P. S. 1981 On the displacement height in the logarithmic velocity profile. *J. Fluid Mech.* **111**, 15–25.

Judd, M. J., Raupach, M. R. & Finnigan, J. J. 1996 A wind tunnel study of turbulent flow around single and multiple windbreaks; Part I: Velocity fields. *Boundary-Layer Met.* **80**, 127–165.

Kim, J. & Moin, P. 1985 Application of a fractional-step method to incompressible Navier–Stokes equations. *J. Comput. Phys.* **59**, 308–323.

Kim, J., Moin, P. & Moser, R. 1987 Turbulence statistics in fully developed channel flow at low Reynolds number. *J. Fluid Mech.* **177**, 133–166.

Krogstad, P.-M. & Antonia, R. A. 1994 Structure of turbulent boundary layers on smooth and rough walls. *J. Fluid Mech.* **277**, 1–21.

Krogstad, P.-M., Antonia, R. A. & Browne, L. W. B. 1992 Comparison between rough- and smooth-wall turbulent boundary layers. *J. Fluid Mech.* **245**, 599–617.

Lee, J. 1996 Modeling boundary layer flows over rough surfaces using a modified Chien k–ε turbulence model. AIAA-96-0384.

Leonardi, S., Orlandi, P., Djenidi, L. & Antonia, R. A. 2003*a* Structure of turbulent channel flow with square bars on one wall. In *Proc. Third Intl Symp. on Turbulence and Shear Flow Phenomena*, vol. 1, pp. 123–128. Sendai, Japan.

Leonardi, S., Orlandi, P., Smalley, R. J., Djenidi, L. & Antonia, R. A. 2003*b* Direct numerical simulations of turbulent channel flow with transverse square bars on the wall. *J. Fluid Mech.* **491**, 229–238.

Ligrani, P. M. & Moffat, R. J. 1986 Structure of transitionally rough and fully rough turbulent boundary layers. *J. Fluid Mech.* **162**, 69–98.

Miyake, Y., Tsujimoto, K. & Nakaji, M. 2001 Direct numerical simulation of rough-wall heat transfer in a turbulent channel flow. *Intl J. Heat Fluid Flow* **22**, 237–244.

Moser, R. D., Kim, J. & Mansour, N. N. 1999 Direct numerical simulation of turbulent channel flow up to $Re_\tau = 590$. *Phys. Fluids* **11** (4), 943–945.

Nagano, Y., Hattori, H. & Houra, T. 2004 DNS of velocity and thermal fields in turbulent channel flow with transverse-rib roughness. *Intl J. Heat Fluid Flow* **25**, 393–403.

Nikuradse, J. 1933 Strömungsgesetze in rauhen Rohren. *Forschungsheft Arb. Ing.-Wes.* **361**.

Novak, M. D., Warland, J. S., Orchansky, A. L., Ketler, R. & Green, S. 2000 Comparison between wind tunnel and field measurements of turbulent flow. Part I: Uniformly thinned forests. *Boundary-Layer Met.* **95**, 457–495.

Perry, A. E. & Joubert, P. N. 1963 Rough-wall boundary layers in adverse pressure gradients. *J. Fluid Mech.* **17**, 193–211.

Perry, A. E., Schofield, W. H. & Joubert, P. N. 1969 Rough wall turbulent boundary layers. *J. Fluid Mech.* **37**, 383–413.

Perry, A. E., Henbest, S. M. & Chong, M. S. 1986 A theoretical and experimental study of wall turbulence. *J. Fluid Mech.* **165**, 163–199.

Poggi, D., Porporato, A., Ridolfi, L., Albertson, J. D. & Katul, G. G. 2004*b* The effect of vegetation density on canopy sub-layer turbulence. *Boundary-Layer Met*. **111**, 565–587.

Poggi, D., Katul, G. G. & Albertson, J. D. 2004*b* Momentum transfer and turbulent kinetic energy budgets within a dense model canopy. *Boundary-Layer Met*. **111**, 589–614.

Raupach, M. R. 1981 Conditional statistics of Reynolds stress in rough-wall and smooth-wall turbulent boundary layers. *J. Fluid Mech.* **108**, 363–382.

Raupach, M. R. & Shaw, R. H. 1982 Averaging procedures for flow within vegetation canopies. *Boundary-Layer Met*. **22**, 79–90.

Raupach, M. R., Antonia, R. A. & Rajagopalan, S. 1991 Rough-wall turbulent boundary layers. *Appl. Mech. Rev*. **44**, 1–25.

Raupach, M. R., Finnigan, J. J. & Brunet, Y. 1996 Coherent eddies and turbulence in vegetation canopies: the mixing layer analogy. *Boundary-Layer Met*. **78**, 351–382.

Rogers, S. E. & Kwak, D. 1990 Upwind differencing scheme for the time-accurate incompressible Navier–Stokes equations. *AIAA J*. **28**, 253–262.

Schlichting, H. 1979 *Boundary-Layer Theory*, 7th edn. McGraw–Hill.

Seo, J.-M. 2004 Closure modeling and numerical simulation for turbulent flows: wall roughness model, realizability and turbine blade heat transfer. PhD thesis, Stanford University.

Shafi, H. S. & Antonia, R. A. 1997 Small-scale characteristics of a turbulent boundary layer over a rough wall. *J. Fluid Mech.* **342**, 263–293.

Shah, K. B. & Ferziger, J. H. 1998 Large eddy simulations of flow past a cubic obstacle. PhD thesis, Stanford University.

Spalart, P. R. 1987 Hybrid RKW3 + Crank–Nicolson scheme. *Internal Rep*. NASA-Ames Research Center, Moffett Field, CA.

Spalart, P. R. & Allmaras, S. R. 1994 A one-equation turbulence model for aerodynamic flows. *Rech. Aérosp*. **1**, 5–21.

Tennekes, H. & Lumley, J. L. 1972 *A First Course in Turbulence*. MIT Press.

Wilson, N. R. & Shaw, R. H. 1977 A higher order closure model for canopy flow. *J. Appl. Met*. **16**, 1198–1205.

Yang, K. & Ferziger, J. H. 1993 Large-eddy simulation of turbulent obstacle flow using a dynamic subgrid-scale model. *AIAA J*. **31**, 1406–1413.

Zhuang, Y. & Wilson, J. D. 1994 Coherent motions in windbreak flow. *Boundary-Layer Met*. **70**, 151–169.